

VOLCANOLOGY

Fracturing and tectonic stress drive ultrarapid magma flow into dikes

Freysteinn Sigmundsson^{1*}, Michelle Parks², Halldór Geirsson¹, Andrew Hooper³, Vincent Drouin², Kristín S. Vogfjörd², Benedikt G. Ófeigsson², Sonja H. M. Greiner^{1,4,5}, Yili Yang¹, Chiara Lanzi¹, Gregory P. De Pascale¹, Kristín Jónsdóttir², Sigrún Hreinsdóttir⁶, Valentyn Tolpekin⁷, Hildur María Friðriksdóttir², Páll Einarsson¹, Sara Barsotti²

Many examples of exposed giant dike swarms can be found where lateral magma flow has exceeded hundreds of kilometers. We show that massive magma flow into dikes can be established with only modest overpressure in a magma body if a large enough pathway opens at its boundary and gradual buildup of high tensile stress has occurred along the dike pathway prior to the onset of diking. This explains rapid initial magma flow rates, modeled up to about 7400 cubic meters per second into a dike ~15-kilometers long, which propagated under the town of Grindavík, Southwest Iceland, in November 2023. Such high flow rates provide insight into the formation of major dikes and imply a serious hazard potential for high-flow rate intrusions that propagate to the surface and transition into eruptions.

Stress has a major influence on the geometrical form and widening of dikes in Earth's crust, which are pathways for magma ascent. Uncertainties remain, however, on what governs the timescale of dike formation. In extensional tectonic settings, regional dikes are often vertical and aligned approximately perpendicular to the direction of the minimum compressive stress. In oblique spreading zones, a component of shearing on dikes is observed (1). In volcanic systems, stresses are also influenced by the local magmatic architecture. At divergent plate boundaries, tectonic stress is released by intruding dikes, fed by underlying magma sources either from the mantle or within the crust. In some cases, the buildup of pressure in such sources can be inferred from geodetic measurements that reveal prediking inflation (2). The criterion for failure of magma bodies in the crust is uncertain; some models consider tensile failure and crustal tensile strength of about 1 to 10 MPa (3), whereas others assume shear failure by faulting that requires overpressure in magma bodies (pressure in excess of ambient pressure in the crust) with substantially higher values, on the order of tens of MPa (4). Thus, the level of overpressure in dike-feeding magma bodies is uncertain. Knowledge of these thresholds would enable better use of geodetic observations at volcanoes in forecasting future eruptions.

Because flow in subsurface magma channels in the crust is driven by pressure gradients,

high overpressure in a source can explain high flow rates. However, if the tensile failure criterion is appropriate, it severely limits the overpressure that can form in a dike-feeding source. An alternative way to drive massive flow is when extensional processes have lowered the minimum compressional stress in the crust where the dike will form and the initial magma pathway emanating from a feeding magma source has a sufficiently large cross-sectional area. Our modeling of geodetic observations indicated that this was the case when a ~15-km-long dike formed rapidly in November 2023 in the Svartsengi volcanic system on the Reykjanes Peninsula in Iceland and partly propagated under the town of Grindavík, causing widespread damage and evacuation of the local population (Fig. 1).

The process of diking is associated with characteristic ground deformation and sometimes surface fracturing and faulting (1, 5–8). These can be mapped and modeled to infer the shape and amount of opening in a dike. The location of a magma source feeding the dike may also be revealed through ground deflation. On 10 November 2023, a linear trend of migrating seismicity and associated ground deformation revealed a dike propagating rapidly from below the Sundhnúkur crater row on the Reykjanes Peninsula, passing under the town of Grindavík (referred to as the Grindavík dike) and extending under the ocean floor. This was concurrent with deflation of the nearby Svartsengi area, a central volcanic complex, which, along with an extensive fissure swarm, forms the Svartsengi volcanic system (9). The area hosts a high-temperature geothermal field where the Blue Lagoon geothermal resort is located. The deflation occurred in an area where five inflation episodes occurred in the 2020 to 2023 period prior to the Grindavík dike (10–12). These events are a part of an ongoing period of volcano-tectonic

activity on the Reykjanes Peninsula (1, 13, 14). The Grindavík dike continued to expand at low rates for days following its formation, and inflation began in the same area where co-diking deflation occurred when the dike formed. This inflation continued until 18 December 2023, when a diking event and fissure eruption occurred on the northern part of the Sundhnúkur crater row. The vigor of the eruption increased rapidly over a few hours as eruptive fissures opened over a distance of ~4 km, then activity quickly declined, and the eruption ended 21 December after forming a ~3.5-km² lava flow. Following a similar increase in pressure over 3 weeks, another diking event and eruption occurred from 14 to 16 January 2023, when lava flowed into the town of Grindavík.

For the Svartsengi area, studies of crustal seismic velocities have revealed velocity anomalies consistent with partially molten magma pockets or a magma reservoir. Seismic ambient noise tomography (15) inferred an anomaly with low seismic velocities between 3- and 6-km depth at the location of the Svartsengi geothermal field, interpreted to be the heat source of the geothermal activity. Studies of the most recent eruptive products in the Svartsengi system from 1210 to 1240 CE infer magma storage at 7- to 10-km depth (16). The Sundhnúkur crater row previously erupted ~2350 years ago, when magma passed through an inferred zone of weakness (17). We analyzed the Grindavík dike formation and the inflation and deflation of the Svartsengi area between 27 October and 12 November 2023 for a better understanding of the physical processes involved.

Geodetic and seismic observations and interpretation

Three-dimensional ground deformation was well resolved both temporally and spatially with dense Global Navigation Satellite System (GNSS) geodetic observations (figs. S1 to S9), and interferometric analysis of synthetic aperture radar images (InSAR) was done by using Sentinel-1, COSMO-SkyMed, and ICEYE satellites (figs. S10 to S12). Seismicity recorded by the National Seismic Network of Iceland (SIL), operated by the Icelandic Meteorological Office, showed the key features of events (Fig. 1 and figs. S13 to S16). Geodetic modelling was carried out (by using data explained below), assuming sources of deformation within a uniform elastic half space (18).

Seismicity increased substantially in the Svartsengi area on 25 October 2023, followed by a new inflation period beginning on 27 October 2023 (figs. S4 and S5). Geodetic modeling (18–20) suggested a sill-shaped intrusive volume at ~5-km depth, with an average volume increase rate of ~7.5 m³/s until 10 November 2023, when an accumulated volume of ~9 × 10⁶ m³ was inferred (Fig. 2). The depth estimate placed the pressure increase near the

¹Nordic Volcanological Center, Institute and Faculty of Earth Sciences, University of Iceland, IS-102 Reykjavík, Iceland.

²Icelandic Meteorological Office, IS-105 Reykjavík, Iceland.

³COMET, School of Earth and Environment, University of Leeds, Leeds LS2 9JT, UK. ⁴Department of Earth Sciences, Uppsala University, 752 36 Uppsala, Sweden. ⁵Center for Natural Hazard and Disaster Science, 752 36 Uppsala/Stockholm/Karlstad, Sweden. ⁶GNS Science, Lower Hutt 5011, New Zealand. ⁷ICEYE OY, Maarinne 6, 02150 Espoo, Finland.

*Corresponding author. Email: fs@hi.is

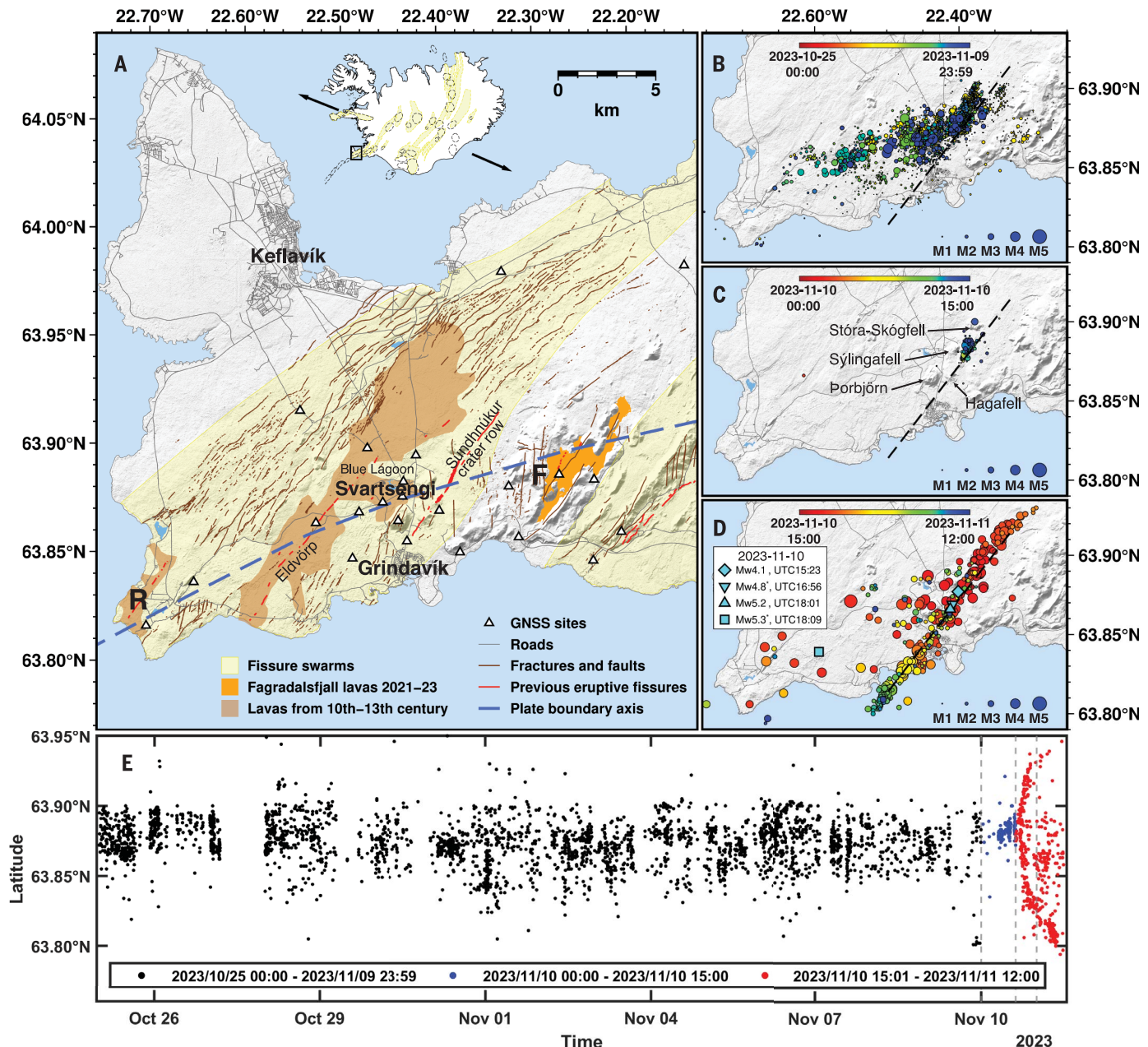


Fig. 1. Location map and seismicity. (A) Western part of the Reykjanes Peninsula showing the Svartsengi, Reykjanes (R), and Fagradalsfjall (F) volcanic systems; fractures (52); Fagradalsfjall lavas (53, 54); fissure swarms (55); lava fields from the 10th to the 13th century (56); plate boundary axis (I); and background digital elevation model (57). At the top, Iceland is shown with fissure swarms (yellow areas), central volcanoes (dashed ovals), and far field-spreading direction (58). The Reykjanes Peninsula is marked with a black rectangle. Previous eruptive fissures shown are those from the 10th to the 13th century (55) and the Sundhnúkur crater row eruption from ~2350 years ago (17). (B) Reviewed seismicity from the Icelandic Meteorological Office VI/SIL database (25) during the inflation period, 27 October to 9 November, colored according to time of occurrence and showing the ~3-km-wide band of seismicity following the trend of the plate boundary. The surface projection of the dike

emplaced on 10 November is shown by the dashed line. (C) Seismicity from 00:00 to 15:00 on 10 November. (D) Dike seismicity from 15:01 on 10 November to 12:00 on 11 November, showing the full extent of the dike and seismicity in the Svartsengi area. Events mentioned in the text are identified in the plot. Star-marked magnitudes are from the German Research Center for Geosciences GFZ GEOFON moment-tensor solutions. Blue circles of increasing sizes represent earthquake magnitudes. (E) Time evolution of seismicity with latitude showing propagation to the north and south on 10 November. Seismicity before 15:00 on 10 November is shown in blue and thereafter in red. The last vertical hatched gray line marks midnight on 10 November. Because only a fraction of the seismicity has been reviewed, the events appear to be episodic, with gaps in between, although the activity was continuous throughout the whole period.

local brittle-ductile boundary on the basis of depth distribution of seismicity and inferred plate-boundary locking depth (27–23). Between January 2020 and June 2022, four inflation episodes occurred in Svartsengi, and one ad-

ditional period of uplift occurred in 2021 in relation to activity at Fagradalsfjall and along the plate boundary (fig. S2). Corresponding deformation data for these earlier events could also be explained with sill-shaped intrusions, with

a total volume increase of 9×10^6 to $11 \times 10^6 \text{ m}^3$ for the first three periods (12, 13), and an additional volume of $\sim 4 \times 10^6 \text{ m}^3$ for the inflation period in 2022 (figs. S17 to S18). From 25 October to 9 November 2023, seismicity occurred with

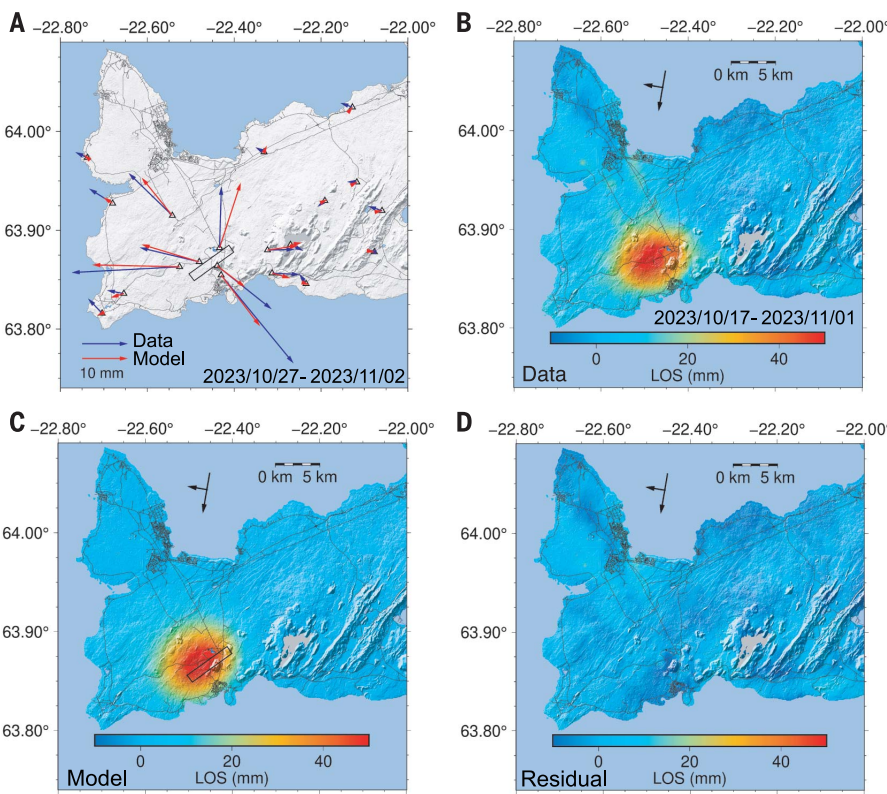


Fig. 2. Inflation at Svartsengi, 27 October to 10 November. (A) GNSS displacements, observed and modeled. The triangles show the locations of GNSS stations used in geodetic modeling. The rectangle indicates the surface projection of the modeled sill that best fits observations. (B) Line-of-sight (LOS) displacement of unwrapped COSMO-SkyMed interferogram. Arrows indicate the satellite heading (long arrow) and look direction (short arrow). (C) Predicted line-of-sight displacement. (D) Residuals [the difference between observations (B) and model predictions (C)].

varying intensity in location and with time, extending from the Sundhnúkur crater row in the east and across the Svartsengi geothermal area to Eldvörp crater row in the west, with additional more-distant triggered earthquakes along the plate boundary (Fig. 1B). In the central part of the activity, several strike-slip earthquakes on north-south-oriented faults of moment magnitudes (M_w) >4 occurred on multiple faults. Throughout this period, seismicity beneath the Sundhnúkur crater row was most intense on the second day (26 October).

Around 7:00 UTC on 10 November 2023, rapid low-magnitude seismicity, typical of subsurface magma migration (24), started at 4- to 6-km depth under Sundhnúkur crater row, gradually moving 3.5 km northward to Stóra-Skófelli over the next 8.5 hours (Fig. 1C and figs. S13 to S16). We did not detect surface deformation signals during this time. Southward migration of the seismicity commenced after a M_w 4.1 event at 15:23; thereafter, seismic propagation occurred both to the north and the south (Fig. 1E). The propagation to the south was faster, and the events much larger than on the northern segment. At 16:56, a M_w 4.8 earthquake occurred just north of Mt. Hagafell,

and more events immediately followed. At 18:01, a M_w 5.2 event occurred at Hagafell, followed by a continuous swarm of small and large events that advanced at a fast pace toward Grindavík. By 18:30, the events had reached the town of Grindavík, and by 19:30, earthquakes were detected south of the town. From just before noon on 10 November until midnight, around 25 $\geq M_w$ 4 earthquakes occurred, two of which were of $\sim M_w$ 5.2. At 16:40, deformation commenced at high rates as detected by the GNSS network (Fig. 2 and fig. S7). Horizontal and vertical deformation reached 1 m by 20:00, after which deformation rates and seismicity decreased. The temporal evolution of GNSS displacements shows that the northeast part of the dike expanded first, followed by the southwest part (fig. S6), which was in broad agreement with development of seismicity. Dike-induced extension was accommodated at the surface along dike-subparallel normal faults and fissures forming near Svartsengi and south, toward the coast, including the town of Grindavík (fig. S19).

Geodetic modeling constrained by an interferogram using a COSMO-SkyMed satellite image acquired 19:35 on 10 November, about

3 hours after the onset of surface movements, and GNSS displacements for the same period (Figs. 3 and 4 and fig. S20) revealed that the dike volume at that time was already $\sim 70 \times 10^6$ to $80 \times 10^6 \text{ m}^3$. Further modeling incorporating line-of-sight offsets, calculated from ICEYE, COSMO-SkyMed, and Sentinel-1 synthetic aperture radar (SAR) satellite images, together with GNSS data up until 19:00 on 12 November, indicated a dike volume of 130×10^6 to $139 \times 10^6 \text{ m}^3$ (Fig. 4 and fig. S21). The model had up to $\sim 8\text{-m}$ opening at 2- to 4-km depth, as well as some strike-slip displacement. Deflation at Svartsengi in our model was best fit using a spherical point source (20) at a depth of 4.0 to 4.2 km, with a volume decrease of 76×10^6 to $82 \times 10^6 \text{ m}^3$ until 12 November.

We further modeled the temporal evolution of the dike opening using hourly GNSS displacements (25), allowing better derivation of the temporal evolution of the flow rate into the dike and the contraction volume of the subsidence source (Fig. 5 and figs. S22 to S25). The numbers derived from the modeling with GNSS data alone were scaled to give the same cumulative volume as inferred from GNSS and SAR data, as the hourly dike models derived by using only GNSS data as the input had greater uncertainty. The maximum flow rate into the dike was inferred to be $\sim 7400 \text{ m}^3/\text{s}$ between 19:00 and 20:00 on November 10.

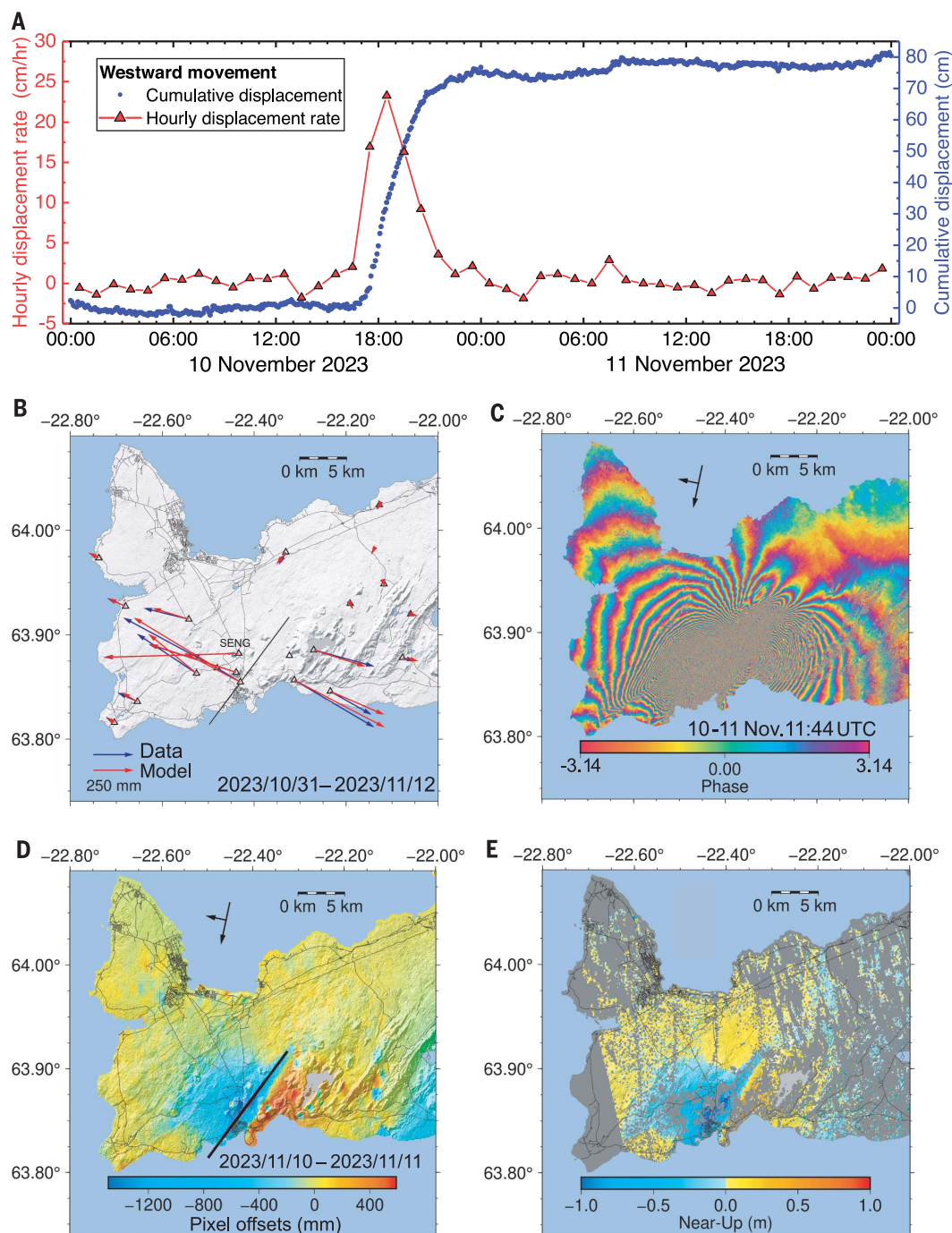
Physical model

The deflation of the Svartsengi magma source from 10 to 12 November amounted to $\sim 80 \times 10^6 \text{ m}^3$, whereas the cumulative inflation volume over the five inflow periods during 2020 to 2023 amounted to $\sim 23 \times 10^6 \text{ m}^3$. GNSS measurements in the Svartsengi area back to 1993 (22) show no inflation episodes prior to 2020 (fig. S2). Because the timescales of the November 2023 prediking inflation and codiking deflation were days or weeks, we inferred that elastic response dominated during them, with pressure change scaling linearly with the amount of ground deformation. The volume ratio of $\sim 23/80 = 0.29$ gave a maximum value for the ratio of preeruptive pressure increase to co-eruptive pressure drop. If any relaxation of stress occurred between the inflation episodes prior to 10 November, the ratio would have been even lower. This called for a physical model in which the cumulative prediking pressure increase was modest; otherwise, an unrealistically large codiking underpressure (pressure less than ambient crustal pressure) would have been inferred. The Kilauea 2018 caldera collapse occurred after a pressure drop of $\sim 17 \text{ MPa}$ (26), with a comparable value inferred at Bárðarbunga in 2014 (27), which can be taken as an upper bound on the observed underpressure required to trigger a caldera collapse in basaltic volcanic settings. No caldera collapse occurred in the events studied at

Fig. 3. Geodetic observations of the dike formation.

(A) Hourly displacement rate and cumulative displacement time series from GNSS station SENG [labeled in (B)]. (B) GNSS displacements, observed and modeled. The shaded background shows topography, and the thin lines represent roads. The triangles show the locations of GNSS stations used in the geodetic modeling. The black line represents the surface projection of the dike. (C) ICEYE interferogram spanning 10 to 11 November at 11:44, with the long and short arrows indicating the flight and line-of-sight directions, respectively. Each color fringe represents 15.5 mm of relative line-of-sight displacement.

(D) Line-of-sight pixel offsets estimated from same images that were used to create (C). The black line represents the surface projection of the dike. (E) Vertical displacements (Near-Up) estimated from ICEYE, COSMO-SkyMed, and Sentinel-1 pixel offset data by combining observations from satellites with different line-of-sight directions (23). More data spanning the dike formation are shown in fig. S11.



Svartsengi, so we considered a preeruptive pressure increase substantially higher than 5 MPa at Svartsengi unlikely.

We tested a physical model (Fig. 5) against observations and inferred a set of approximate values of model parameters, including the amount of pressure increase and decrease in the Svartsengi source and the driving pressure needed for the rapid dike formation. We envisioned that during the Svartsengi inflation episodes, magma was emplaced into a crustal

volume, which we refer to as a magma domain (27, 28), that consisted of liquid magma, partial melt, magma mush, and hot solid rock (Fig. 5). This scenario was consistent with the five-sill inflation models that cover a similar area within a zone of low-seismic velocities. We suggest that the sills correspond to the top of the magma domain at ~5-km depth, which may be larger at levels deeper than the sills' area outline. Although models put the deflation source slightly shallower than the sill em-

placement depth, we suggest that the inferred sills mark the top of the magma domain that deflated. Fitting a point source to observed deformation and assuming a uniform elastic half-space can cause model error that systematically influences depth estimates (29). The seismic velocity anomalies were several kilometers thick, although the actual value is uncertain.

For a fixed volume change, the pressure change in the magma domain depends on its shape and size, its compressibility, and the host rock

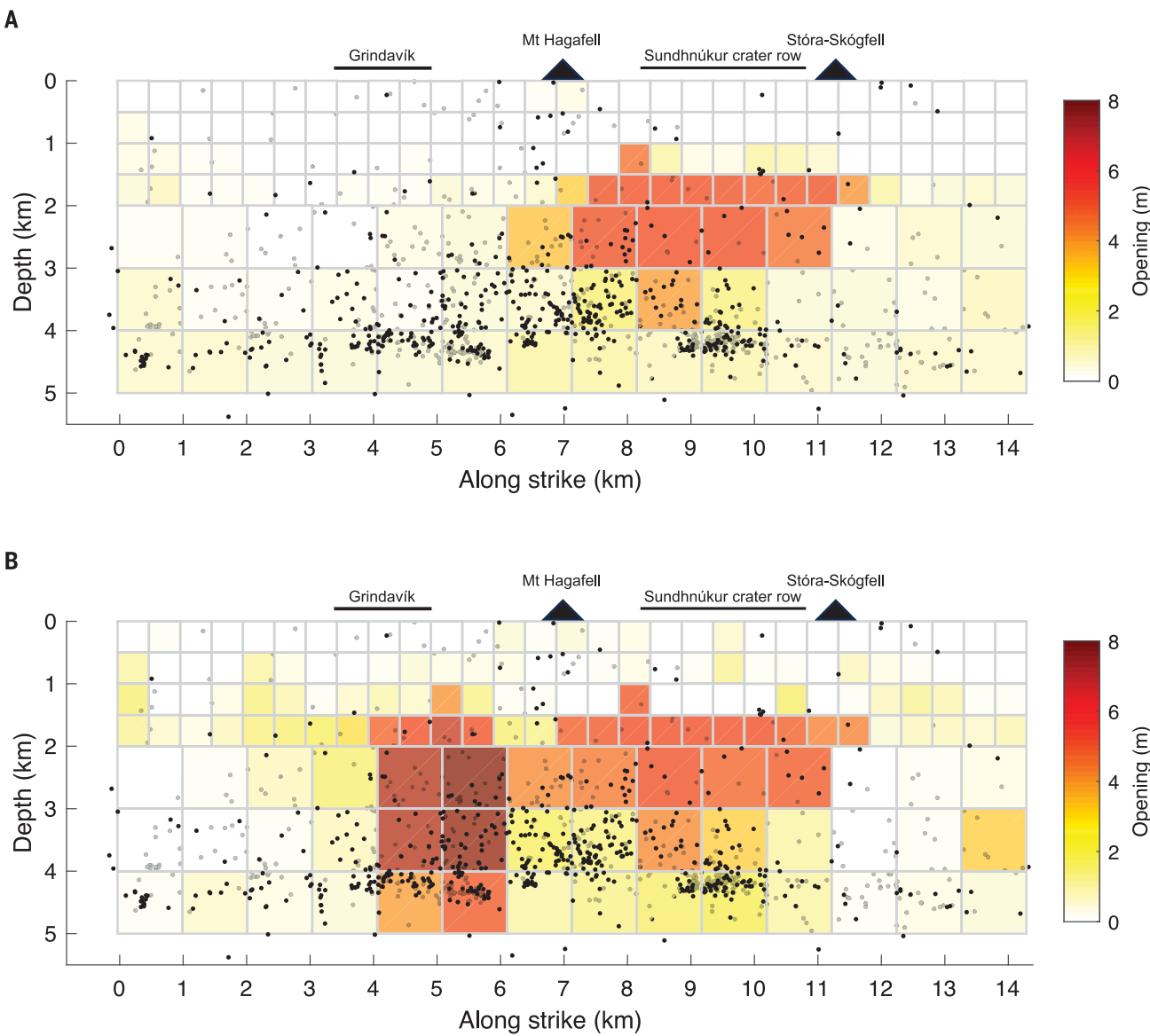


Fig. 4. Geodetic models of dike formation, 10 to 12 November. (A) Median values of dike opening in a model until 19:35 on 10 November. (B) Same as (A), but until 19:00 on 12 November. High-precision relocated seismicity related to the dike is overlain on the model, showing the maximum depth of seismicity matching the depth of the dike intrusion. Black indicates the front (east) of the dike, and gray, behind (west). The surface projection of the dike is shown in Fig. 3B.

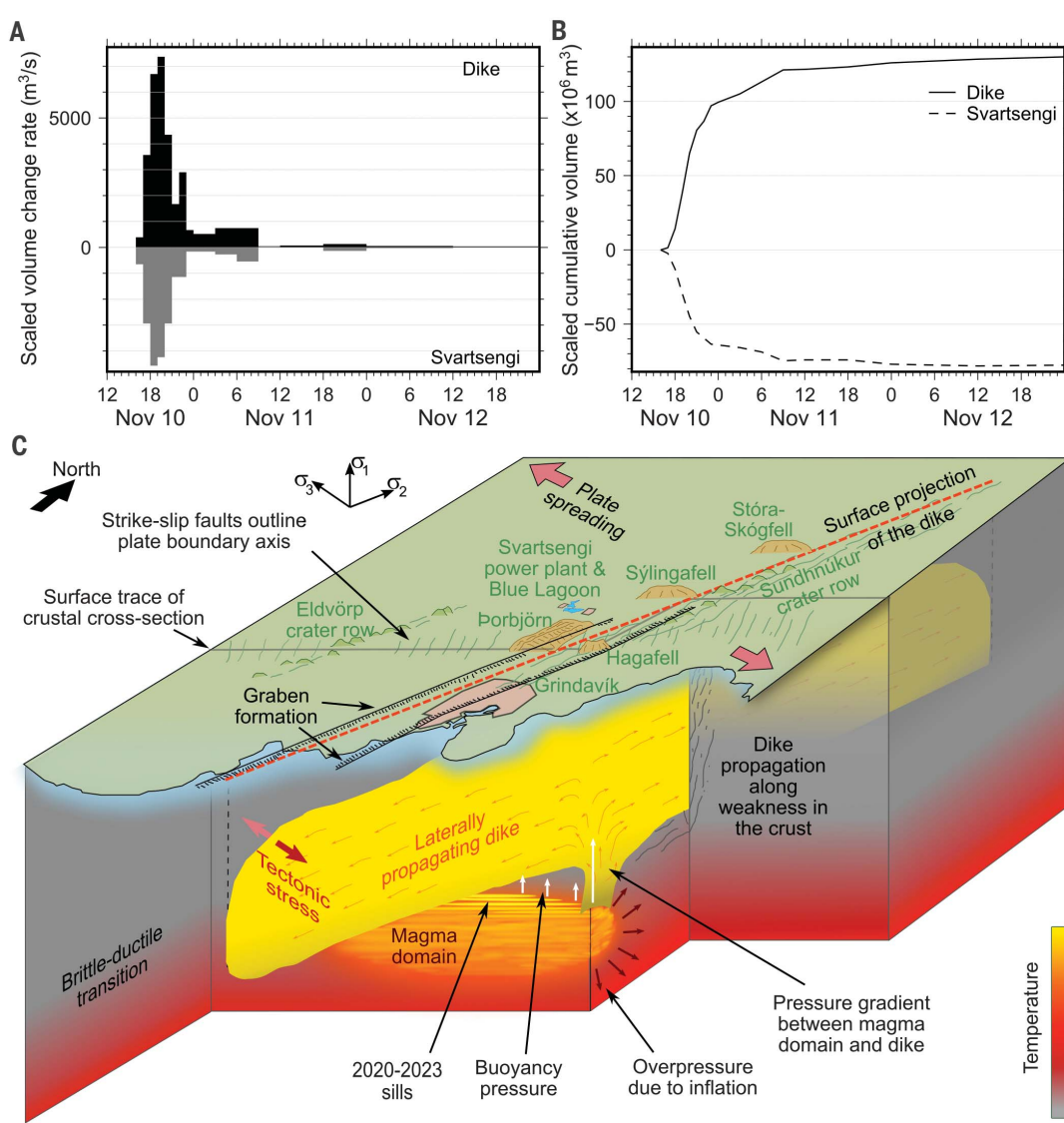
shear modulus (18). A representative magma domain geometry is needed that does not produce unrealistically large underpressure during the deflation and has a cross-sectional area comparable to that of the prediking sills. We used a horizontal oblate spheroid with horizontal semiaxes $a = 4$ km, $b = 1.5$ km, and c (the half-thickness of the magma domain) = 1.5 km. For these numbers and a crustal shear modulus of 10 GPa (25), the pressure drop associated with the inferred 10 to 12 November magma domain deflation volume ($\sim 80 \times 10^6 \text{ m}^3$) was ~ 21 MPa, and for the cumulative inflation volume prior to diking of $\sim 23 \times 10^6 \text{ m}^3$, it was 6 MPa. However, some of the pressure buildup associated with the inflation episodes may have been partly relaxed by viscoelastic or porovisco-

elastic relaxation (30–32). Observed deflation following previous Surtsegi inflations (fig. S2) was consistent with this, and a more representative value for total prediking pressure increase in the magma domain due to inflow may be ~ 4 to 5 MPa, which is in line with the constraint from the absence of caldera collapse.

Buoyancy pressure at the top of the magma domain depends on the vertical extent of connected liquid magma, ΔH , and the density difference between magma and host rock, estimated at a depth of 5 to 8 km to be 300 kg/m^3 (27). Assuming that ΔH is in the range 1 to 3 km (considering magma lenses within the magma domain may not all be connected), then the buoyancy pressure is in the range 3 to 9 MPa. Assuming that long-term stresses due to plate

spreading and glacial isostatic adjustment are completely relaxed below the brittle-ductile boundary, the excess tensile stress on the boundary (hoop stress) is approximately equal to combined pressure increase due to magma inflow and buoyancy pressure (27), or ~ 7 to 14 MPa. We considered this to be the tensile strength reached on 10 November. We interpreted that magma flowed from the magma domain at ~ 5 -km depth into the lower part of the central opening area of the dike and upwards to about 1.5- to 3-km depth, where it spread more laterally (Fig. 4). This is the depth level of neutral buoyancy, where basaltic magma has comparable density to the surrounding crust in Iceland (27, 33). Increase in overpressure during upward migration depends on the average

Fig. 5. Magma flow rates and schematic model. (A) Inferred volume change rate and (B) cumulative volume of the Grindavík dike and the magma domain centered under Svartsengi, based on modeling of GNSS data (25). (C) Illustration of the Grindavík dike and the proposed magma domain under Svartsengi. The magma domain underlies the plate boundary axis (outlined by north-south-striking strike-slip faults) and reaches approximately from the Eldvörp crater row in the west to close to Mt. Hagafell in the east. The Grindavík dike propagated under the northeast-southwest-striking Sundhnúkur crater row in the north and under the town of Grindavík in the south, where a graben formed on 10 November (black lines). Surface projections of the Grindavík dike and the crustal cross section are outlined by red dashed and gray solid lines on the surface, respectively. Illustration is not to scale.



Downloaded from https://www.science.org at University Van Amsterdam on April 13, 2025

difference in density between host rock and magma, estimated here to be 200 kg/m^3 , considering a smaller average difference in density at 2- to 5-km depth than at deeper levels (27). For 3 km of upward flow, the increase in overpressure was $\sim 6 \text{ MPa}$, and the total inferred overpressure was ~ 13 to 20 MPa in the “central zone of lateral divergence” in the upper part of the dike.

We considered further the effect of the tectonic stress. When a dike propagates, its opening will depend on the dike fluid pressure versus the host rock normal stress along the dike plane, both influenced by lithostatic pressure that cancels out. The remaining deviatoric normal stress acting on the dike as a result is primarily from tectonic stress. The excess pressure in the dike is increased by the deviatoric normal stress. When the deviatoric

stress is fully relaxed, the excess pressure is reduced by the amount of deduced deviatoric normal stress (33). If a new patch of dike is opening at the far end of a propagating dike, then the amount of deviatoric normal stress there translates into a component of effective driving pressure for diking. The dilatational stress rate due to plate movement on the Reykjanes Peninsula was about ~ 0.009 to 0.011 MPa/year near the plate boundary axis (7). Since 1240 CE, when the last eruption took place, the amount of accumulated normal stress reduction on the dike plane may have amounted to ~ 7 to 9 MPa . We took this as an estimate of the contribution to the driving stress. This added to the inferred overpressure in the dike at 2-km depth, so the estimated driving pressure for magma flow was ~ 20 to 29 MPa . This is the estimated maximum pos-

sible pressure drop in the magma domain; below this, the driving pressure would fall below zero and magma flow would stop.

The ratio of the dike volume and the contraction volume of the magma domain gave further constraints. For the 10 to 12 November dike and magma domain deflation, the inferred ratio was 1.6 to 1.8. This ratio depends on the shape of the magma domain and the ratio between the shear modulus of host rock and the compressibility of material within the magma domain (34–36). For the magma domain geometry and host rock shear modulus assumed above, as well as the volume ratio derived from our modeling, the inferred compressibility of the magma domain was 0.06 to 0.08 GPa^{-1} (18). The 1.6 to 1.8 volume ratio we found is at the lower end of ratios reported in earlier studies for basaltic systems (34, 36),

and the compressibility value is lower than an estimate for Icelandic basaltic magma (27). This is consistent with the magma domain not being filled with only liquid magma, but rather being a complex of hot solid host rock, liquid magma, and magma mush.

The flow rate in a magma channel is proportional to the driving pressure (ΔP) and inversely proportional to the viscosity (η) of the magma and the length of the channel (L) (37). The flow rate furthermore scales with the cross-sectional area (A) of the channel and a geometrical factor (α) that depends on the geometrical form of the channel and its minimum lateral dimension (38):

$$Q = \alpha \frac{A}{\eta L} \Delta P \quad (1)$$

Here, Q is the volumetric magma flow rate. The driving pressure for the flow depends on pressure conditions at the two ends of a channel. If the effective magma pathway from the magma body to the main dike has a rectangular cross-sectional area of $A = Dw$, where D is the long-side length and w is the short-side length, then the geometrical factor in Eq. (1) is:

$$\alpha_{\text{rectangle}} = \frac{w^2}{12} \quad (2)$$

This equation was used to interpret magma flow in dikes formed in the Krafla rifting episode (39). For a driving pressure of 20 to 29 MPa, representative Icelandic basaltic magma viscosity in the range of 10 to 100 Pa s (40), and flow path length of 5 km, the flow rates we inferred from geodetic modeling can be produced if the effective magma pathway has D in the range 0.5 to 3 km and w in the range of 0.5 to 5 m (fig. S26). Such a range of dike dimensions is commonly found in Iceland (41).

Widening of the narrowest part of the magma channel connecting the magma domain and the main dike body may control the rise time in magma flow toward a peak value. Our geodetic data suggest that this was several hours (Fig. 5). As deflation continues, the effect of the tectonic stress becomes proportionally larger in the driving pressure. The term related to overpressure due to prediking magma inflow disappears quickly, and remaining contributions are due to buoyancy in the magma domain and the upward channel, as well as the tectonic stress. We infer that high tensile stress at the distal ends of a laterally propagating dike is a key feature, as its important contribution to the driving pressure does not decay with time as long as the dike propagates into an area where tensional stress has not been released.

The 18 to 21 December 2023 diking and eruption at the Sundhnúkar crater row was preceded by renewed magma inflow and pressure increase in the Svartsengi magma domain for 5 weeks. Following these events,

pressure gradually increased in the magma domain, and diking and eruption occurred again from 14 to 16 January 2024. By modeling the temporal evolution of magma flow from co-diking GNSS observations as we did for the 10 to 12 November period, the inferred peak magma flow rate into a dike on 18 December was $\sim 800 \text{ m}^3/\text{s}$, and $\sim 1700 \text{ m}^3/\text{s}$ on 14 January. The short-lived nature of the eruptions and rapid decline of pressure in the feeding source during them suggests limited overpressure in the feeding magma domain and rapid draining of magma from it, similar to the November diking.

Implications

Our inferred peak magma flow rate of $\sim 7400 \text{ m}^3/\text{s}$ was two orders of magnitude larger than those inferred for the 2021, 2022, and 2023 diking events in the nearby Fagradalsfjall area (1, 13, 14). The flow rate was also larger than that estimated for the 2014 to 2015 Bárðarbunga events, when a total of $\sim 2 \text{ km}^3$ of magma were emplaced partly within a 48-km-long dike that formed over 2 weeks and partly erupted with an initial inferred magma flow rate of $\sim 240 \text{ m}^3/\text{s}$ (42). However, in the initial half of the Krafla rifting episode of 1975 to 1984, peak magma flow rates into dikes, reached within a few hours of diking onset, were up to 2000 to 3000 m^3/s , as estimated from continuous recording of ground tilt (43). The peak flow rate in the Grindavík dike is comparable to the inferred average eruption rate in the first 12 days of the massive 1783 to 1784 Laki eruption, when 14.7 km^3 erupted in total during an 8-month period (44). Given sufficient supply, once most deviatoric stress is released along a laterally propagating dike, upward flow can result in an eruption with very high discharge rates. However, sustaining high driving pressure over a long duration of time (weeks or more), as occurred at Laki, requires either a much larger volume of magma in the feeding source than at Grindavík, slowing down the pressure drop as magma flows away from it, or caldera collapse, when sometimes large volumes of magma can be extracted into a laterally propagating dike at low-pressure drop rates (26, 42). Furthermore, flow rates are highly dependent on the viscosity of the magma, as well as its density (low density creating high buoyancy). From the Northern Volcanic Zone of Iceland, it was inferred that the majority of post-glacial basaltic magma erupted had viscosity $>30 \text{ Pa s}$ (40).

Our findings have implications for magmatic activity in other parts of the world where extensional processes gradually lower the minimum compressional stress in the crust, such as along the midoceanic ridges of the world, and Afar (East Africa), where incipient sea floor spreading takes place (45). The big-

gest volcano in the Cascades, the Newberry Caldera, has linear vent eruptions related to extension and ample evidence for many non-erupting intrusions (46). However, eruptions only occur around fractures that facilitate migration to the surface (47). Instability of volcano flanks can lead to extensional regimes. In Hawaii, the relationship between reduction in normal stress through volcano flank motion and timing of dike intrusions has been highlighted (48). Modest amounts of overpressure in the prediking or eruptive phase combined with the development of underpressure in magma domains with a range of volumes, plus potential for caldera formation, can explain the range of flow rates and volumes in diking events and eruptions when the effects of tensile deviatoric stress are considered.

Some of the giant dike swarms on Earth ($>300 \text{ km}$ long) may have formed in association with the onset of large igneous provinces and continental breakup in relation to mantle plumes impinging on the lithosphere, such as the Mackenzie dike swarm in Canada and the British Tertiary dike swarm (49, 50). Widespread uplift above an arriving mantle plume head creates tensile stress favorable for lateral diking radiating from a focal point and downslope off a plume-related topographic swell (51). The Grindavík 2023 dike showed how magma flow rates of $>7000 \text{ m}^3/\text{s}$ into a dike can be established when a sufficiently large fracture opens into a magma domain and the magma can flow into an area of high tensile stress. Long-distance lateral propagation is then facilitated if pressure in the magma domain drops slowly, which can be the case if the magma domain is very large, as expected at the onset of large igneous provinces, or if a caldera collapse occurs (26, 42). Other limiting factors for the length of lateral diking are the size of the area of tensional stress, which would be comparable to the size of plume heads prior to rifting above them, and solidification of the magma as it flows in a dike (51). Giant dikes may form over several weeks, with magma flow emanating from a localized magma domain at sustained magma flow rates comparable to that observed on 10 November 2023 in the Grindavík dike.

REFERENCES AND NOTES

1. F. Sigmundsson *et al.*, *Nature* **609**, 523–528 (2022).
2. E. Sturkell *et al.*, *J. Volcanol. Geotherm. Res.* **150**, 14–34 (2006).
3. S. Jónasson, *Geophys. Res. Lett.* **39**, 14–34 (2012).
4. G. Currenti, C. A. Williams, *Phys. Earth Planet. Inter.* **226**, 14–27 (2014).
5. A. M. Rubin, D. D. Pollard, *Geology* **16**, 413–417 (1988).
6. L. G. Mastin, D. D. Pollard, *J. Geophys. Res.* **93**, 13221–13235 (1988).
7. J. S. Pallister *et al.*, *Nat. Geosci.* **3**, 705–712 (2010).
8. F. Sigmundsson *et al.*, in *Volcanic and Igneous Plumbing Systems, Understanding Magma Transport, Storage, and Evolution in the Earth's Crust* (Elsevier, 2018).
9. K. Sæmundsson, M. Á. Sigurgeirsson, G. Ó. Frölefifsson, *J. Volcanol. Geotherm. Res.* **391**, 106501 (2020).

10. H. Geirsson et al., "The 2020 volcano-tectonic unrest at Reykjanes Peninsula, Iceland: stress triggering and reactivation of several volcanic systems," abstract EGU21-E7534 presented at the online EGU General Assembly 2021, 19 to 30 April 2021.
11. Y. Cubuk-Sabuncu et al., *Geophys. Res. Lett.* **48**, e2020GL092265 (2021).
12. Ó. G. Flóvenz et al., *Nat. Geosci.* **15**, 397–404 (2022).
13. M. Parks et al., *Bull. Volcanol.* **85**, 60 (2023).
14. H. Geirsson et al., "Reykjanes Peninsula Unrest and Fagradalsfjall Fires 2020–2023, Iceland: Deformation History of a Multi-Event Rifting Episode in a Trans-Tensional Environment," abstract G41A-05 presented at the 2023 American Geophysical Union Fall Meeting San Francisco, CA, 11 to 15 December 2023.
15. J. E. Martins et al., *J. Volcanol. Geotherm. Res.* **391**, 106685 (2020).
16. A. Caracciolo et al., *Earth Planet. Sci. Lett.* **621**, 118378 (2023).
17. M. H. Jenness, A. E. Clifton, *Bull. Volcanol.* **71**, 715–728 (2009).
18. Materials and methods are available in the supplementary materials.
19. Y. Okada, *Bull. Seismol. Soc. Am.* **75**, 1135–1154 (1985).
20. K. Mogi, *Bull. Earthq. Res. Inst. Univ. Tokyo* **36**, 99–134 (1958).
21. H. Vadon, F. Sigmundsson, *Science* **275**, 193–197 (1997).
22. S. Hreinsdóttir, P. Einarsson, F. Sigmundsson, *J. Geophys. Res.* **106** (B7), 13803–13816 (2001).
23. V. Drouin, F. Sigmundsson, *Geophys. Res. Lett.* **46**, 8046–8055 (2019).
24. E. P. S. Eibl et al., *Nat. Geosci.* **10**, 299–304 (2017).
25. Supplementary text is available in the supplementary materials.
26. K. R. Anderson et al., *Science* **366**, eaaz1822 (2019).
27. F. Sigmundsson et al., *Nat. Commun.* **11**, 2403 (2020).
28. F. Sigmundsson, *Geophys. Res. Lett.* **43**, 12,423–12,427 (2016).
29. R. Foroozan, D. Elsworth, B. Voight, G. S. Mattioli, *Geophys. Res. Lett.* **37**, 2010GL042511 (2010).
30. T. Yamasaki, T. Kobayashi, T. J. Wright, Y. Fukuhata, *J. Volcanol. Geotherm. Res.* **349**, 128–145 (2018).
31. Y. Liao, S. A. Soule, M. Jones, H. Le Mével, *J. Geophys. Res. Solid Earth* **126**, e2020JB019395 (2021).
32. R. Alshembari, J. Hickey, B. J. Williamson, K. Cashman, *J. Geophys. Res. Solid Earth* **128**, e2023JB026625 (2023).
33. E. R. Heimisson, A. Hooper, F. Sigmundsson, *J. Geophys. Res. Solid Earth* **120**, 8774–8792 (2015).
34. E. Rivalta, P. Segall, *Geophys. Res. Lett.* **35**, L04306 (2008).
35. K. Anderson, P. Segall, *J. Geophys. Res.* **116**, B07204 (2011).
36. S. Hreinsdóttir et al., *Nat. Geosci.* **7**, 214–218 (2014).
37. C. Jaupart, in *Encyclopedia of Volcanoes* (Academic Press, 2000), pp. 237–245.
38. F. Sigmundsson, in *Forecasting and Planning for Volcanic Hazards, Risks and Disasters*, vol. 2 of Hazards and Disasters Series, P. Papale, Ed. (Elsevier, 2021), pp. 413–438.
39. P. Einarsson, B. Brandsdóttir, *J. Geophys.* **47**, 160–165 (1980).
40. M. Hartley, J. MacLennan; M. Hartley M and J. MacLennan, *Front. Earth Sci.* **6**, 29 (2018).
41. A. Gudmundsson, in *Physics and Chemistry of dykes* (Balkema, 1995), pp. 23–34.
42. M. T. Gudmundsson et al., *Science* **353**, aaf8988 (2016).
43. E. Tryggvason, *J. Geophys.* **47**, 141–153 (1980).
44. Th. Thordarson, S. Self, *J. Geophys. Res.* **108**, 4011 (2003).
45. T. Wright et al., *Nat. Geosci.* **5**, 242–250 (2012).
46. M. W. Beachly, E. E. E. Hoot, D. R. Toomey, G. P. Waite, *J. Geophys. Res.* **117**, 2012JB009458 (2012).
47. D. McKay, J. Donnelly Nolan, R. Jensen, D. Champion, in *Volcanoes to Vineyards: Geologic Field Trips Through the Dynamic Landscape of the Pacific Northwest, Field Guide*, vol. 15, J. E. O'Connor, R. J. Dorsey, I. P. Madin, Eds. (Geol. Soc. of Am., 2009), pp. 91–110.
48. E. K. Montgomery-Brown, A. Miklius, *Geology* **49**, 397–401 (2021).
49. R. E. Ernst, J. W. Head, E. Parfitt, E. Grosfils, L. Wilson, *Earth Sci. Rev.* **39**, 1–58 (1995).
50. R. E. Ernst, E. B. Grosfils, D. Mege, *Annu. Rev. Earth Planet. Sci.* **29**, 489–534 (2001).
51. Y. A. Fialko, A. M. Rubin, *J. Geophys. Res.* **104** (B10), 23033–23049 (1999).
52. A. E. Clifton, S. A. Kattenhorn, *Tectonophysics* **419**, 27–40 (2006).
53. G. Pedersen et al., *Geophys. Res. Lett.* **49**, e2021GL097125 (2022).
54. S. R. Gunnarson et al., Automated processing of aerial imagery for geohazards monitoring: Results from Fagradalsfjall eruption, SW Iceland, August 2022 (I.O.), version 1, Zenodo (2023); <https://doi.org/10.5281/zenodo.7701194>.
55. H. Jóhannesson, K. Sæmundsson, Geological map of Iceland 1:600,000—Tectonics. Icelandic Institute of Natural History, Reykjavík (2009).
56. H. Jóhannesson, K. Saemundsson, Geological Map of Iceland—Tectonics, 1:500,000. Icelandic Institute of Natural History, Reykjavík (1998).
57. LMI, (2022). Landmælingar Íslands. Available at: <https://www.lmi.is/is/um-lmi/frettafirlit/ny-upplaerla-a-haedarlakni-af-islandi>.
58. D. F. Argus, R. G. Gordon, C. DeMets, *Geochem. Geophys. Geosyst.* **12**, 11 (2011).
59. M. Parks et al., Data and geodetic modelling results for "Fracturing and tectonic stress drives ultra-rapid magma flow into dikes," OSF (2024); <http://osf.io/9rcq7>.

ACKNOWLEDGMENTS

We thank two anonymous reviewers for comments that helped to improve the manuscript and Á. Rut Hjartardóttir for help in making Fig. 1. We thank the Institute of Geophysics, the Czech Academy of Sciences, and the Iceland GeoSurvey for allowing access to data acquired from seven of their seismic stations [currently running under the NASPMON project Reykjane (2022)] connected to the monitoring system of the Icelandic Meteorological Office (IMO) to improve the detection and routine locations of earthquakes, as well as the use of data from three

of these stations (lag, Ife, and iss) in the relative relocations of seismicity along the dike. We thank the IMO and University of Iceland technicians for support and operation of the GNSS and seismic stations. The diligence and support from the Natural Hazards Specialists (on duty in the IMO monitoring room) and IMO's seismic analysts is appreciated. We also thank participants of various science and evaluation meetings held in connection to the Reykjanes unrest and the National Commissioner of the Icelandic Police and their Department of Civil Protection. The Geohazard Supersites and Natural Laboratory (GSNL) Icelandic Volcanoes Supersite project supported by the Committee on Earth Observing Satellites is acknowledged for providing access to satellite data that were used in this study. We thank the GEO-GSNL initiative for its ongoing support of InSAR monitoring and research in Iceland. COMET is the UK NERC Centre for the Observation and Modelling of Earthquakes, Volcanoes, and Tectonics. **Funding:** This research was supported by the Icelandic Research Fund (grant nos. 228933-051 and 239615-051); the University of Iceland Research Fund; the H2020 DEEPVOLC project, funded by the European Research Council (grant no. 866085); and the CHEESE-2P Horizon 2021 EuroHPC JU-RIA project (GA no. 101093038). The NASPMON (natural seismicity as a prospecting and monitoring tool for geothermal energy extraction) project benefits from a grant from Iceland, Liechtenstein, and Norway through the EEA Grants and the Technology Agency of the Czech Republic within the KAPPA Programme. **Author contributions:** F.S. and M.P. coordinated the writing of the paper and the development of the ideas presented. Geodetic modeling and interpretation were carried out by A.H., M.P., V.D., and C.L. GNSS observations and analysis were carried out by H.G., B.G.Ó., S.H., Y.Y., and H.M.F. InSAR analysis was carried out by V.D. and V.T. Seismic analysis was done by K.S.V., supported by K.J. Analysis of graben formation was led by G.P.D.P. The evaluation of the implications of the study of volcanic hazards was led by S.B.. All authors contributed to the evaluation of the modeling, the discussion of the results, and the writing of the paper. S.H.M.G. created Fig. 5C; S.H.M.G., Y.Y., and C.L. compiled Figs. 1 to 3. **Competing interests:** The authors declare no competing interests. **Data and materials availability:** All data are available in the main text, supplementary materials, and (59). **License information:** Copyright © 2024 the authors, some rights reserved; exclusive licensee American Association for the Advancement of Science. No claim to original US government works. <https://www.science.org/about/science-licenses-journal-article-reuse>

SUPPLEMENTARY MATERIALS

science.org/doi/10.1126/science.adn2838

Materials and Methods

Supplementary Text

Figs. S1 to S28

References (60–70)

Submitted 2 December 2023; accepted 29 January 2024

Published online 8 February 2024

10.1126/science.adn2838